Antifogging Properties of Spinodal Porous Structures for Optical Application

Zuyi Zhang*

Read Online

ACCESS | 📊 Metrics & More | 📖 Article Recommendations

ABSTRACT: For the optical applications of antifogging, equilibrium amounts of adsorbed water with humidity were measured on bulk glasses having spinodal pores of 4, 10, 15, 20, and 50 nm. The kinetics of adsorption toward a saturated state and desorbing reversely from the saturated state were investigated on a 15 nm sample that was etched sufficiently to suppress the influence of the silica gel left in the pores. To clarify the role of the pores, the relative humidity (RH) was transformed to Kelvin's diameter, φ. There were pronounced hysteresis loops in the adsorption amounts against humidity, in which adsorption occurred at higher humidities and desorption took place at humidities corresponding to sizes of pores confirmed by mercury intrusion porosimetry. On the basis of weather data in Tokyo, the antifogging coating having pores larger than 12 nm in size was proposed with an emphasis on the recovery of antifogging. Antifogging was further discussed in terms of the capabilities of adsorption related to the thickness of the porous layer and the kinetics of adsorption with a degree of supersaturation at RH100%.

Antifogging mechanism based on spinodal pores

Kelvin's diameter
$$\varphi = -\frac{4\gamma V_m}{RT \ln\frac{P}{P_0}}$$
$$\frac{\varphi_{ab}}{\varphi_{de}} = \sim 1.7$$

$\varphi_{de} \sim 12\,nm$
$RH \sim 82\%$

Adsorption

Desorbing of water

Adsorbing of water

φ_{de} φ_{ad} φ
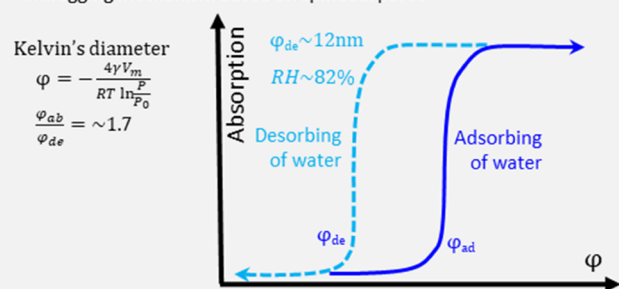
INTRODUCTION

In imaging systems, antireflection (AR), dust proof, and antifogging properties are considered fundamental factors for high-quality images.[1] Antifogging coating based on absorbent polymers has been used on the surface of the eyepiece in a finder imaging system that suffers from the moisture of the user's breath.[2] In normal imaging systems, the use of such polymer coatings is limited. There is a concern of deterioration in surface flatness with the rapid adsorption of moisture, since blistering tends to occur in these polymers due to their soft nature.[3]

Several antifogging coatings based on nanostructures have been reported. A polymer coating was etched to form a structure of nanograsses by self-masking reactive ion etching,[4] and a worm-like structure was prepared by calcinating polyacrylate/polypropylsilsesquioxane coating at 500 °C.[5] Nanoporous thin films prepared by a layer-by-layer assembly of silica particles and other materials[5−7] have been reported to show both antireflection and superhydrophilic wetting. A nanoporous silica layer of 500 nm thickness was also prepared directly onto a silicate glass by a simple one-pot etching.[8] On the other hand, attempts have been also made to develop low-refractive-index coatings[9] with the purpose of depressing the formation of ghosts and flares. Okuno reported a subwavelength structure (SWS) coating consisting of a texture of crystalline AlOOH platelets 220 nm in size.[10] Murata reported a sol−gel MgF$_2$ porous layer for AR,[11] which had a refractive index of 1.18. Tanaka et al. proposed a glass mold for preparing a moth-eye structure directly on the surface of the glass lens, which had a low

reflectivity of 0.2% at 520 nm.[12] Moth-eye structures were also prepared on silica and spinel ceramic substrate for near-infrared laser systems through UV lithography and dry etching, in which high thresholds of up to 100 J/cm^2 were achieved.[13] These textured surfaces are considered to contribute to superhydrophilic wetting as well. Although these as-prepared coatings show both antifogging and antireflection, the refractive index increases and antireflection probably diminishes with the adsorption of moisture into the structures. In fact, to the best of our knowledge, even with controlled textures on the surface, antifogging property tends to be low and diminishes on exposure to ambient atmosphere, probably due to adsorption of organic species from the air.

As a systematic approach, we reported a coating film of porous structure for optical applications based on the phase separation of borosilicate glass. An interface structure shown in Figure 1 was effective in achieving an antireflection of ∼0.5%.[14] In another serial paper, it was confirmed that the pores absorbed oil (nonvolatile liquid) without losing the antireflection.[15] Such a layer is capable of absorbing liquid water and was applicable to
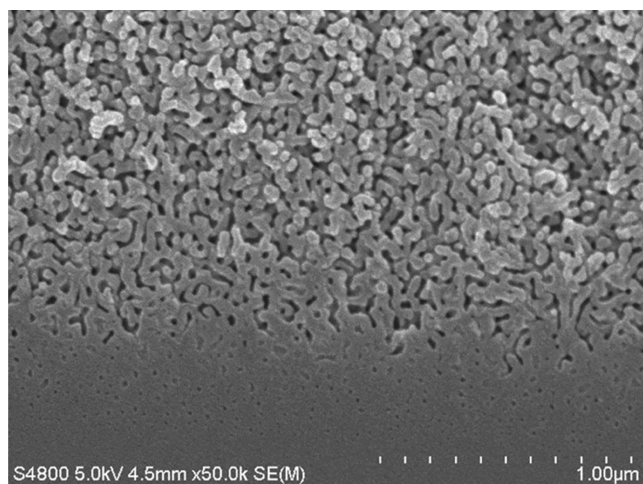
Figure 1. Scanning electron microscopy (SEM) micrograph of a cross section of a substrate with an antireflection coating based on spinodal phase separation [ref 14]. The average reflection in the visible region from the coating was 0.5−0.6%.

antifogging, and the mechanism is indicated in Figure 2. When the temperature dropped to the dew point, excessive water
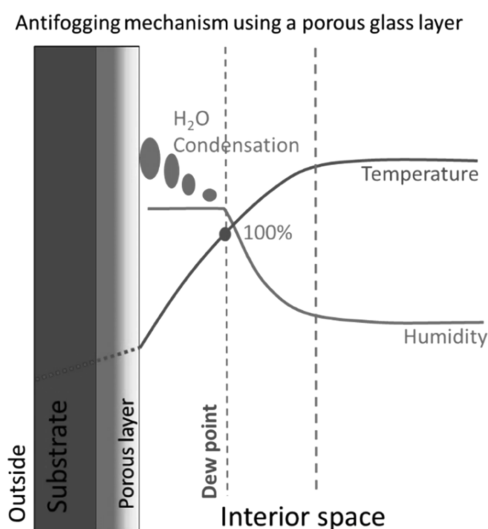
Figure 2. Mechanism of antifogging coating based on a porous layer. When an optical window suffers a decrease in temperature, the relative humidity near the substrate increases. As the relative humidity increases, the porous layer starts to adsorb water, instead of forming drops of water on the surface. The porous layer is thick enough to accommodate excessive water generated from the interior space, keeping the effective dew point in the neighborhood of coated surface below the practical temperature.

nearby could be incorporated into the porous film, leaving the surface free of drops of water. Pores of the coating were tens of nanometers in size, and the ratio of the thickness to the size of pores reached 200−400. Therefore, the coating probably resembled a bulk in the adsorption behavior. In the present study, for the accuracy of the amount of adsorption, bulks of porous silica having a thickness of ∼1 mm were used to investigate the adsorption/desorption in contact with a circumstance with the precisely controlled relative humidity (RH).

EXPERIMENTAL SECTION

Glass with a composition of Na_2O, B_2O_3, SiO_2, and Al_2O_3 was provided by Akagawa Glass Company (Osaka). The glass composition was designed so that it was capable of forming porous structures having pore sizes from 10 to 20 nm, and porosities up to 65% after phase separations at temperatures from 530 to 600 °C. First, the glass was melted at 1400 °C, poured into a mold, and then annealed at 400−550 °C. A block thus obtained was allowed to phase separate at about 540 °C for 80 h with an aim of 15 nm. Two other glasses with aims of 10 and 20 nm were prepared by setting the phase separation times to 25 h (hours) and 200 h, respectively. After phase separations, the glass blocks were cut into plates with a size of 3 cm × 3 cm × 1 mm, and two sides of the plates were polished to an optical grade. The surface roughness (Ra) prior to the etching was estimated to be 0.6−1 nm according to the conditions of polishing. For comparison, a glass with an aim of 50 nm was prepared from a composition that was modified by changing the content of Al_2O_3 and the phase separation at 600 °C. Etching conditions of the phase-separated plates are described in Table 1 as well as those of the

Table 1. Description of Preparation Conditions of Etching and Measurements of SEM and Adsorption/Desorption[a]

preparation of samples			measurements		
	etching, 90 °C			water contents, 25 °C	
ϕ	acid	period	SEM	equilibria	kinetics
50 nm	0.5 M H_2SO_4 500 mL	20 h	yes	40−99% (RH)	
15 nm		20 h			
		72 h	No		adsorbing at 98%, 96%, 94% (RH)
					desorbing at 85%, 80%, 70% (RH)
10 nm					
20 nm					
4 nm	unknown				

[a]The sample of 4 nm was a Corning's vycor glass (no. 7930). Kinetics of adsorption/desorption were measured on a 15 nm sample prepared by etching for 72 h.

subsequent experiments. As the normal condition of the etching, each phase-separated glass was etched in 500 mL of 0.5M H_2SO_4 with stirring at 93 °C for 20 h. For comparison, a vycor glass (Code No. 7930) with a pore size of 4 nm was purchased from Gikenkagaku. As to the nanopores of 15 and 50 nm samples, surfaces and cross sections were observed with a scanning electron microscope (FE-SEM S-4800, Hitachi). In a series of 10, 15, and 20 nm samples, the etching period was extended to 72 h to minimize the influence of silica gel, which was formed due to the low solubility of silica in acid.[14] All pore sizes (ϕ) aimed by the mentioned conditions were expressed according to mercury intrusion porosimetry.

Prior to the adsorption experiments, three samples were heat-treated at 200 °C for 5 h; these were considered as references of the dehydrated states. For adsorption and desorption processes, two series of experiments were performed using an environmental test chamber (Espec, PL-2J), in which the plates of porous glasses were placed directly on a Teflon tray in a semi-infinite fashion. First, to obtain equilibrium adsorption amounts as a function of humidity, the samples were kept at 25 °C in various humidities from RH33% to RH99% for 10 h or overnight, and the weights were measured in less than 10 s (seconds) using an electronic balance (Asone, IBA-200) with an error of ±0.2 mg. Of the equilibrium states, it was confirmed that there were no remarkable changes after exposures beyond 10 h under several typical conditions. Second, the kinetics of the adsorption of a 15 nm sample was investigated by exposure to RH94%, RH96%, and RH98% with time steps of 30 min and 1 h toward a saturated state, whereas that of the desorption from the saturated state was monitored by exposing to RH70%, RH80%, and RH85%, respectively.

For convenience, the humidities are transformed to Kelvin's diameters by the following equation

$$\varphi = -\frac{4\gamma V_m}{RT \ln \frac{P}{P_0}} \tag{1}$$

where φ is Kelvin's diameter, γ is the surface tension of water, and V_m molecular volume of liquid water. R, T, and P/P_0 are gas constant, absolute temperature, and relative humidity, respectively.

■ RESULTS

Figure 3 shows equilibrium adsorption amounts for three glasses of 4 nm (vycor), 15, and 50 nm (20 h) during both adsorption
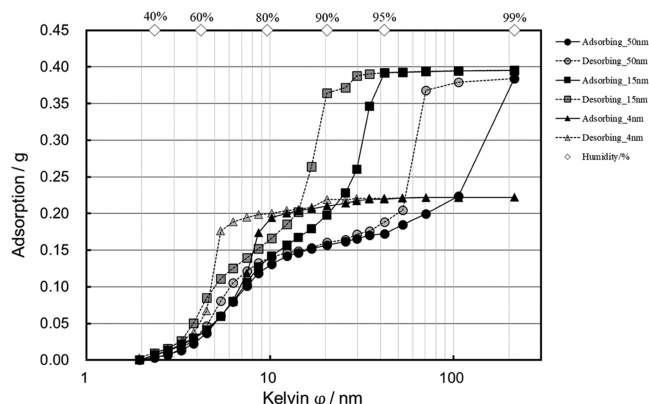
Figure 3. Equilibrium amounts of adsorption of water as a function of Kelvin diameter for samples of 50, 15, and 4 nm (vycor glass). Kelvin diameters are transformed from humidities using eq 1.

and desorption procedures from RH33% to RH99%, in which weights at RH33% were used as the references. The adsorption amounts failed to follow the same curves during the two procedures and showed hysteresis loops. For example, in the sample of 50 nm, the equilibrium adsorption amount increased sharply above 100 nm (RH98%) with the increasing humidity but dropped remarkably between 50 and 70 nm (RH96% to RH97%) with the decreasing humidity. In a sample of 15 nm, the loop was also distinct in the region from 15 to 30 nm. Below RH80%, however, the loops became less notable in both samples, although adsorptions up to one-third of the total amounts occurred in this region. In addition, the vycor glass also showed a well-developed hysteresis from 4 to 8 nm.

As for the states of adsorption, two preliminary experiments were carried out on the three glasses. First, prior to the adsorption experiments, the weights in the dehydrated states (heat-treated at 200 °C) were measured. The results are shown

in Table 2, with those at RH40% and RH99%, and the differences in the weight (ΔW) between RH40% and RH99%. Second, the three glasses were inserted directly into distilled water, and then their weights were also measured after taking out and removing drops of water at corners with a clean paper. It was found that the weights were essentially the same as those observed at RH99%. The volumes corresponding to the skeletons and the pores were calculated for all of the samples using densities of 2.2 and 1 g/cm³ for the skeletons and adsorbed water, respectively, and the results are also included in Table 2 (see Discussion).

Figure 4 shows the SEM micrographs of 15 and 50 nm samples. In Figure 4A, both surfaces give well-developed

(A) Surfaces exposed to etching

(B)
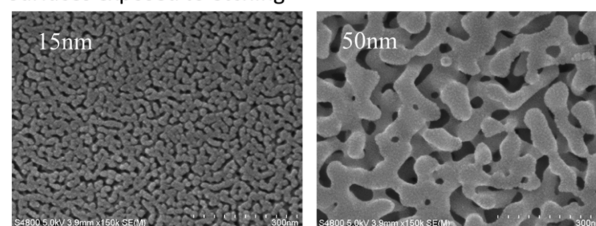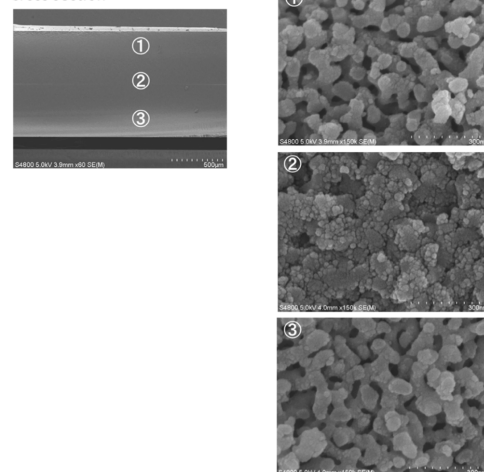
Figure 4. (A) SEM micrographs of the surfaces of the 15 and 50 nm samples subjected to etching. (B) SEM micrographs of the cross section of the 50 nm sample. Numbers in the left micrograph denote the areas for the right ones with high magnifications.

spinodal skeletons, which suffer direct contact with acid during etching. Figure 4B shows the SEM micrographs of the cross section of the 50 nm sample. Much silica gel is left in the

Table 2. Characteristic Amounts of Adsorption for the Spinodal Porous Samples[a]

samples	weight (g)			ΔW (g) RH40% → 99%	calculated volume (cm³)		
	200 °C 5H (dehydrated)	RH40%	RH99% (saturated)		skeleton	H₂O	total
Vycor 4 nm	1.130	1.185	1.407	0.222	0.514	0.277	0.891
15nm_20H	1.063	1.110	1.505	0.395	0.483	0.442	0.925
50nm_20H	1.127	1.146	1.530	0.384	0.512	0.403	0.915
10nm_72H		0.889	1.315	0.426	0.404		0.830
15nm_72H		0.838	1.381	0.543	0.381		0.924
20nm_72H		0.800	1.343	0.543	0.364		0.907

[a]The weights of the samples in the three states [heat-treated at 200 °C (dehydrated state), RH40% and RH99% (saturated state)], and the changes in the adsorption amount (ΔW) from RH40% to RH99% are shown in left columns. The volumes of silica skeleton, adsorbed water in saturated states, and the total ones are included in the right columns.

intermediate region, which results from the low solubility of silica in acid.[14,17] Cross section of the 15 nm sample was also investigated (not shown), but the SEM images were unaffordable for distinguishing the state of pores, probably because of a fact that the size of silica colloids falls into the same range as those of the silica skeletons and the pores.

Figure 5 shows the equilibrium amounts of adsorption of water for the series of 10, 15, and 20 nm, in which silica colloids
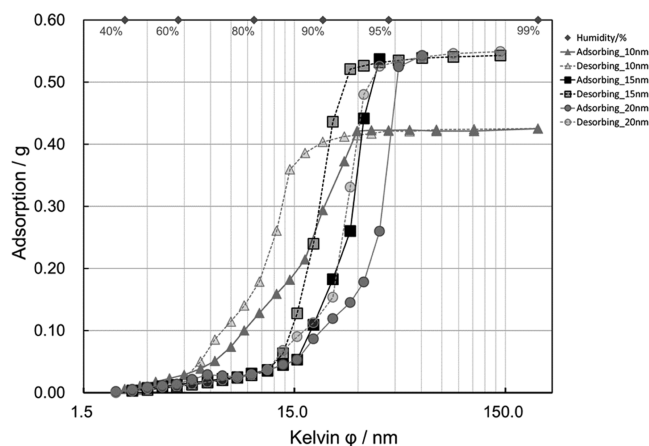
Figure 5. Equilibrium amounts of adsorption of water as a function of Kelvin's diameter for 10, 15, and 20 nm samples prepared by prolonged etching.

are removed to lesser degrees by prolonged etching. Each of them shows a well-developed loop. In 15 and 20 nm samples, the adsorption from 4 to 8 nm is suppressed, and the shoulders in the region of 15−30 nm are still notable during the adsorption procedure. As mentioned above, the equilibrium weights at RH40% and RH99% and the changes in weight are included in Table 2.

The kinetics of both adsorption and desorption of the 15 nm sample were investigated up to 6 H, and the results are shown in Figure 6. During the two procedures, linear regions were noted in the adsorption amounts with time. The kinetics fluctuated in the first hour of the adsorption process. In the desorption process, some tails appeared at later stages toward new equilibrium states on exposure to lower humidities.
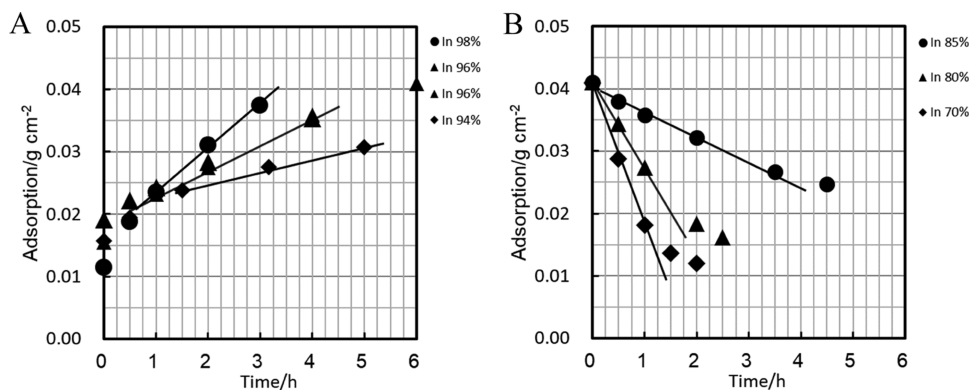
■ DISCUSSION

In porous materials, there is always the issue of mechanical strength, especially from the point of view of capillary force.[18] In mesoporous silica, attempts were made to improve the strength of the powder by hydrothermal treatment, enlarging pores by templets, etc.[19,20] As to the mechanism, a minus pressure of $-4\gamma/\phi$ is caused in the adsorbed water and acts on silica skeletons as compressive stress expressed by eq 2.

$$\sigma = -\frac{1-\eta}{\eta}\frac{4\gamma}{\phi} \tag{2}$$

where σ is the compressive stress of silica skeletons at the side of the occupied region, η is the occupancy ratio of skeletons, γ is the surface tension of water, and ϕ is the diameter of the pores. Corresponding to such a shrinking force, there is a tensile force outside the occupied region. During drying or adsorption, this tends to induce the destruction of the porous structure at the interface between occupied and unoccupied regions.

By comparison with the sol−gel materials such as mesoporous silica, etc., spinodal porous silica affords a larger ϕ, lowering σ. If $\phi = 15$ nm, σ is estimated to be -30 MPa. In addition, the skeletons of silica essentially consist of Q^4 units,[21] other than those of sol−gel materials, which certainly contain a fraction of Q^2 and Q^3 units. During etching, the SiO_2 component in the phase of borate glass is released immediately, giving rise to a saturation concentration of SiO_2 in acid and the formation of silica colloids. This plays a role in keeping the silica skeletons from deteriorating. Namely, the skeletons of silica probably undergo little change during etching and resemble high-temperature silica in structure. In addition, the stress caused by the capillary force is considerably low compared with the mechanical strength of the silica glass.[22] These factors may account for the strength of spinodal silica.

Of silica gel in pores, silica colloids are brought out slowly by acid during the etching. Because of the thickness of 1 mm, the silica colloids tend to be left in the deep region, as seen in Figure 4B. When a comparison is made between weights of the two 15 nm samples in Table 2, a reduction (silica gel) of 0.272 g at RH40% caused by prolonged etching results in an increase of 0.148 g in the adsorbed water (ΔW) in the saturated states. In this case, water replaces the silica gel removed. By assuming a density of 1 g/cm^{3} for the adsorbed water, silica gel is estimated to have an average density of 1.8 g/cm^{3}. If the volume of adsorbed water (0.047 g) at RH40% relative to the dehydrated state is taken into consideration, silica particles in the gel are

Figure 6. Adsorption amounts of water in the 15 nm sample as a function of time. (A) Adsorption toward the saturated state when kept in humidities higher than the threshold of RH93%. (B) Adsorption with time when exposed to lower humidities from the saturated state.

expected to have a net density of 2.2 g/cm^3. It is very close to that of silica glass. Hence, under the present etching conditions, silica particles in the pores (Figure 4B) seem quite dense too. Furthermore, irrespective of the dehydration and the adsorption/desorption processes, all the porous glasses essentially give the same equilibrium amounts of water against φ (humidity), unless the direction of the variation of humidity is changed. All phenomena strongly suggest that little hydration (Si−O−Si + H$_2$O → Si−OH + HO−Si) occurs either on the surface of the silica skeletons or in the silica gel under ambient conditions. For convenience, volumes of both silica (silica skeletons + silica particles) and pores (=volumes of the maximum adsorptions of water) were calculated and the results are listed in the right columns of Table 2. As to the three samples exposed to prolonged etching, adsorbed water below RH40% was disregarded.

On the basis of the above arguments, the changes in weight against humidity are exclusively ascribed to either condensation or desorption of water within pores, in which spinodal pores are responsible for the loops of the adsorptions. Values of φ, extrapolated from the upper regions of the desorbing curves, are found to be in good agreement with the sizes of pores (ϕ) expected by mercury intrusion porosimetry, by which all of the conditions of phase separation are decided.

The apparent size of pores varies due to the precipitation of silica colloids, and silica colloids themselves also form little pores. In Figure 3, the adsorption in the region of 4−8 nm in the 15 and 50 nm samples coincides with the distinct loop in the vycor glass. In fact, much colloidal silica was formed in early vycor glasses,[23,24] where it played a role in the subsequent densification as the silica component. Therefore, the accumulation of silica colloids is responsible for the adsorption of 4−8 nm. With the progress of etching, silica colloids are brought out by acid, few silica colloids are deposited onto the wall of silica skeletons during drying. A schematic model is described in Figure 7. That is, the apparent pore size decreases from φ to φ',
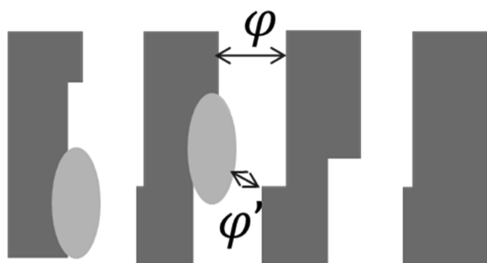
Figure 7. Illustration of influence of silica gel on spinodal pores. The apparent diameter of pores varies from φ to φ' due to the precipitation of silica particles formed during etching.

where φ' may be expressed as $\varphi - d$, and d is the diameter of silica colloids. The shoulders that were noted in the adsorption curves of 15 and 20 nm samples in Figure 5 are ascribed to the contributions of φ'.

It should be mentioned that nanopores are usually investigated by mercury intrusion and low-temperature nitrogen adsorption, respectively. Here, it is clearly demonstrated that the equilibrium amounts of water against φ provide the quantitative information of pores as a function of size.

According to the serial paper,[15] oil from greases was absorbed in the region of the interface of the porous layer due to an increased capillary force, where the pores were terminated or

some silica colloids might be left after etching. A similar situation existed for the adsorption of water in the intermediate region in Figure 4B and in the narrowed pores in Figure 7. Namely, the linear changes in the adsorption amount with time in Figure 6 were characteristic of spinodal pores. However, the fluctuation behaviors deviating from the linearity at an early stage in Figure 6A and at a later stage in Figure 6B are ascribed to contributions from the narrowed pores. On this assumption, the level of liquid water moved gradually depending on the adsorption amount in the linear regions. However, a mechanism of vapor diffusion across the unoccupied region was excluded from rate-determining because it failed to explain such linear relations. The ad/desorbing behavior was tentatively attributed to diffusion in the neighborhood of surface,[25] as expressed by eqs 3 and 4. The driving force arose from the difference in the chemical potential between the vapor state in circumstance, μ_g, and the liquid state in spinodal pores, μ_p.

$$\mu_g = \mu_0 + RT \ln H \quad \mu_p = \mu_{\text{pore}} \tag{3}$$

$$J = -Bc\frac{\mu_p - \mu_g}{t_c} = \frac{Bc}{t_c}(\mu_0 + RT \ln H - \mu_{\text{pore}}) \tag{4}$$

where μ_0 is the standard chemical potential of liquid water, H is the relative humidity, J is the transport of water, B is the mobility of water driven by the chemical potential gradient, c is the concentration of water contributing to diffusion, and t_c is the critical thickness of the diffusion. Once the vapor of water condenses on the surface, the water moves through the porous structure quickly, probably via a flow on the wall of silica skeletons, an effect of the capillary force.

Based on this assumption, the velocities of adsorption per surface area were calculated from the slopes, and are plotted as a function of ln H in Figure 8. There are thresholds of RH93% and
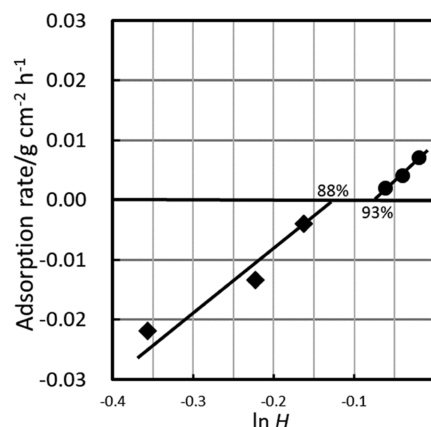
Figure 8. Adsorption rates as a function of ln H in the 15 nm sample prepared by prolonged etching. Values of 93 and 88% are obtained by extrapolating, indicative of the threshold humidities for the two processes.

RH88% for adsorption and desorption, respectively, which correspond to Kelvin's diameters of 29 and 17 nm, respectively. A similar phenomenon has been noted as the "ink bottle effect" in concrete,[26] which is qualitatively explained as the existence of smaller openings for accessing larger voids in interconnected pores. Here, in a precise sense, the diameter of 29 nm limits the complete wetting of the structure during adsorption, whereas that of 17 nm restricts drainage from the saturated state. This

seems understandable from the feature of spinodal pores in Figure 5.

As for the demand for antifogging in Figure 2, the porous layer should remain empty of water until an increase in humidity. Above a critical humidity, it starts to accommodate excessive water as much as possible from the atmosphere to keep the dew temperature under practical temperature. On the other hand, once the porous layer has adsorbed water, it is desirable for the porous layer to recover with a decrease in humidity.

Maximum humidity at night and minimum in the daytime are taken into consideration to design the pores of coating. Weather data of most cities in Japan are available.[27] In Tokyo, most of the maximum humidity observed at night is lower than RH93%. On the other hand, the minimum humidity drops beyond RH80% under normal conditions even during the rainy season. For desorbing water below RH80%, a pore larger than 12 nm is necessary, as shown in Figure 5. If the recovery is emphasized, a porous coating with a diameter of pores larger than 12 nm is considered suitable for the antifogging in Tokyo. For applications elsewhere, the diameter needs to be adjusted according to the respective conditions of humidity. With the same reference of mercury intrusion porosimetry, the requirement for suppressing the adsorption is more attainable due to the "ink bottle effect". Ratios of $\varphi_{ad}/\varphi_{de}$ are analyzed from the curves of adsorption and desorption in the middle region of the loops for the 15 and 20 nm samples in Figure 5 and the 15 nm sample in Figure 3, and all of them give a value of ~1.7. Here, the $\varphi_{ad}/\varphi_{de}$ is regarded as a measure of the "ink bottle effect" for the ideal spinodal pores. Namely, the diameter of the pores can be designed according to increased humidities at night on the basis of $\varphi_{ad}/\varphi_{de}$.

As for the control of spinodal pores, two phases are coarsened during the phase separation, and the size of the silica skeleton, L, varies with time, t, following a relationship $L \sim \sqrt[3]{t}$,[16] which is derived by the interface energy between the two phases. In fact, the three samples of 10, 15, and 20 nm are obtained by adjusting the period of phase separation. For the 15 nm sample (15nm_72H), Table 2 provides an occupancy ratio of silica skeletons of ~41% from the respective volumes (0.381/0.924). L is estimated to be 11.7 nm based on the SEM micrograph in Figure 4A, following a calculation method in ref 15. From these parameters, an average width of pores of ~16.8 nm ($11.7 \times \frac{59\%}{41\%}$) is obtained, in good agreement with the results of the adsorption in Figures 5 and 8. Meanwhile, to the best of our knowledge, the ratio of $\varphi_{ad}/\varphi_{de}$ is essentially unchanged, provided the phase-separated glasses undergo etching smoothly.

The thickness of the porous coating film in ref 14 ranged from 2 to 7 μm. Such thicknesses make it easy for silica colloids to be extracted during etching, which is seen in the SEM microscopy images in Figure 1. In the practical application of the antifogging coating, thickness × porosity should be large enough to accommodate excessive water arising from the interior space in Figure 2 when subject to a drop in temperature outside. For example, for a change in circumstance condition from 15 °C and RH70% to 0 °C and RH100%, 3.4 g of water is generated per m^3 on the basis of the psychrometric chart. Based on the porosity of 65%, the capability of the antifogging is inferred to be ~19 cm/μm, which means that 1 μm of the porous layer accommodates excessive water caused from a space of ~19 cm in depth.

In Figure 8, a maximum adsorption rate of ~0.01 g/cm^{-2} h^{-1} can be expected by extrapolating the adsorption line to RH100%

(ln H = 0). This is equivalent to a rate of ~2.5 μm/min for the movement of liquid water into the porous coating.

■ CONCLUSIONS

The adsorption/desorption of water with the spinodal pores was investigated on the bulks of porous glasses having a thickness of 1 mm. The 15 nm sample, which was obtained by the prolonged etching, showed threshold humidities of RH93% and RH88% during adsorption and desorption, respectively. Ideal spinodal structures gave favorable loops, which were characterized by the $\varphi_{ad}/\varphi_{de}$ ratio of ~1.7 and resembled the "ink bottle effect" in the literature.

For the application of an antifogging coating in Tokyo, pores larger than 12 nm in size were inferred effective, which keeps the pores empty of water under normal conditions and further allows them to recover in ambient circumstances after the adsorption of water. In the case study, a porosity of 65% in the antifogging coating was estimated to give an adsorption capability of 19 cm/μm.

■ AUTHOR INFORMATION

Corresponding Author

Zuyi Zhang − *Nanomaterials Development Department 11, Nanomaterials R&D Center, R&D Headquarters, Canon Inc., Tokyo 146-8501, Japan;* Present Address: Future Technology R&D Center, R&D Headquarters, Canon Inc., 30-2, Shimomaruko 3-chome, Ohta-ku, Tokyo 146-8501, Japan; ◉ orcid.org/0000-0002-2955-8337; Email: zhang.zuyi@mail.canon

Complete contact information is available at:
https://pubs.acs.org/10.1021/acs.langmuir.2c00415

Notes

The author declares no competing financial interest.

■ REFERENCES

(1) INOMATA, T. Evaluation of Optical Thin Films and Development of Functional Thin Film Materials. *J. Surf. Finish. Soc. Jpn.* **2020**, *71*, 613−619.

(2) Canon Inc., 2022, https://cweb.canon.jp/camera/eos/accessary/detail/2200b001.html.

(3) Ueki, K. Diffusion in and Permission through Paint Films. *Kobunshi* **1967**, *16*, 596−600.

(4) Wang, Y.; Ye, X.; Li, B.; He, J.; Zheng, W. Straightforward Approach to Antifogging, Antireflective, Dual-function, Nanostructured Coating. *Langmuir* **2019**, *35*, 11351−11357.

(5) Yuan, J.; Yan, S.; Zhang, X. Superhydrophilic antifogging broadband antireflective coatings with worm-like nanostructures fabricated by one dip-coating method and calcination. *Appl. Surf. Sci.* **2020**, *506*, No. 144795.

(6) Cebeci, F. C.; Wu, Z.; Zhai, L.; Cohen, R. E.; Rubner, M. F. Nanoporosity-driven superhydrophilicity: a means to create multifunctional antifogging coatings. *Langmuir* **2006**, *22*, 2856−2862.

(7) Xu, L.; He, J. Antifogging and Antireflection Coatings Fabricated by Integrating Solid and Mesoporous Silica Nanoparticles without Any Post-Treatments. *ACS Appl. Mater. Interfaces* **2012**, *4*, 3293−3299.

(8) Fujima, T.; Futakuchi, E.; Tomita, T.; Orai, Y.; Sunaoshi, T. Hierarchical Nanoporous Glass with Antireflectivity and Super-hydrophilicity by One-Pot Etching. *Langmuir* **2014**, *30*, 14494−14497.

(9) Kikuta, H. New Technologies for Reduction of Light Reflection. *Jpn. J. Opt.* **2011**, *40*, 2−10.

(10) Okuno, T. The Development of Subwavelength Structure Coating and Its Application to Camera Lenses. *Jpn. J. Opt.* **2011**, *40*, 11−16.

(11) Murata, G. Development of Super-High Performance Antire-flective Coatings Using Fluoride Nanoparticles. *Jpn. J. Opt.* **2011**, *40*, 17−23.

(12) Tanaka, Y.; Tamura, T.; Nishii, J. Molded Glass Lens with Anti-Reflective Structure. *Jpn. J. Opt.* **2011**, *40*, 30−32.

(13) Busse, L. E.; Florea, C. M.; Frantz, J. A.; Shaw, L. B.; Aggarwal, I. D.; Poutous, M. K.; Joshi, R.; Sanghera, J. S. Anti-reflective surface structures for spinel ceramics and fused silica windows, lenses and optical fibers. *Opt. Mater. Express* **2014**, *4*, 2504−2515.

(14) Zhang, Z. Antireflective film of porous silica. *J. Opt. Soc. Am. A* **2022**, *39*, 1172−1178.

(15) Zhang, Z. Dust proof properties of spinodal porous surfaces. *J. Opt. Soc. Am. A* **2022**, *39*, 866−873.

(16) Tanaka, H.; Yazawa, T.; Eguchi, K.; Nagasawa, H.; Matsuda, N.; Einishi, T. Precipitation of colloidal silica and pore size distribution in high silica porous glass. *J. Non-Cryst. Solids* **1984**, *65*, 301−309.

(17) Tanaka, H.; Yazawa, T.; Eguchi, K. Nonuniform Deposition of Silica Gel in High Silica Porous Glass. *J. Ceram. Soc. Jpn.* **1983**, *91*, 384−386.

(18) Eguchi, K.; Uetsuki, T.; Tarumi, S. Swell or Shrinkage of Borosilicate Glass during Acid Leaching. *J. Ceram. Soc. Jpn.* **1979**, *87*, 558−564.

(19) Zhao, D.; Feng, J.; Huo, Q.; Melosh, N.; Fredrickson, G. H.; Chmelka, B. F.; Stucky, G. D. Triblock Copolymer Syntheses of Mesoporous Silica with Periodic 50 to 300 Angstrom Pores. *Science* **1998**, *279*, 548−552.

(20) Thomann, F. S.; Hall, M. R.; Mokaya, R.; Stevens, L. A. Hydrothermal simulation-informed design of mesoporous desiccants for optimised energy efficiency of mixed mode air conditioning systems. *J. Mater. Chem. A* **2015**, *3*, 17290−17303.

(21) Saiki, K.; Sakida, S.; Benino, Y.; Nanba, T. Phase separation of borosilicate glass containing sulfur. *J. Ceram. Soc. Jpn.* **2010**, *118*, 603−607.

(22) Sajzew, R.; Limbach, R.; Wondraczek, L. Deformation and Fracture of Silica Glass Fiber Under Sharp Wedge-Indentation. *Front. Mater.* **2020**, *7*, No. 126.

(23) Vogel, W.; Kreidl, N. J.; Lense, E. *Chemistry of Glass*; American Ceramic Society: Columbus, Ohio, 1985.

(24) Haller, W.; Blackburn, D. H.; Wagstaff, F. E.; Charles, R. J. Metastable Immiscibility Surface in the System Na_2O-B_2O_3-SiO_2. *J. Am. Ceram. Soc.* **1970**, *53*, 34−39.

(25) Kingery, W. D.; Bowen, H. K.; Uhlmann, D. R. *Introduction to Ceramics*; Wiley, 1976; p 220.

(26) Ishida, T.; Chaube, R. P.; Kishi, T.; Maekawa, K. Modeling of Pore Water Content in Concrete under Generic Drying Wetting Conditions. *Doboku Gakkai Ronbunshu* **1997**, *35*, 199−209.

(27) Jpn. Meteorological Agency, 2022, https://www.data.jma.go.jp/gmd/risk/obsdl/index.php.

📖 Recommended by ACS

Molecular Dynamics and Surface Interactions of Nickelocene Adsorbed on Silica: A Paramagnetic Solid-State NMR Study

Jordon W. Benzie, Janet Blümel, *et al.*

JUNE 08, 2022
LANGMUIR   READ 🗗

Determining Mechanical Moduli of Disordered Materials with Hierarchical Porosity on Different Structural Levels

Gudrun Reichenauer, Bernd M. Smarsly, *et al.*

JULY 28, 2022
LANGMUIR   READ 🗗

Structure of Water at Hydrophilic and Hydrophobic Interfaces: Raman Spectroscopy of Water Confined in Periodic Mesoporous (Organo)Silicas

Benjamin Malfait, Denis Morineau, *et al.*

FEBRUARY 09, 2022
THE JOURNAL OF PHYSICAL CHEMISTRY C   READ 🗗

HSIL-Based Synthesis of Ultracrystalline K,Na-JBW, a Zeolite Exhibiting Exceptional Framework Ordering and Flexibility

Karel Asselman, Eric Breynaert, *et al.*

JUNE 15, 2022
CHEMISTRY OF MATERIALS   READ 🗗

Get More Suggestions >